

# Atomistic Kinetic Monte Carlo Study of Atomic Layer Deposition Derived from Density Functional Theory

Mahdi Shirazi and Simon D. Elliott\*

To describe the atomic layer deposition (ALD) reactions of  $\text{HfO}_2$  from  $\text{Hf}(\text{N}(\text{CH}_3)_2)_4$  and  $\text{H}_2\text{O}$ , a three-dimensional on-lattice kinetic Monte-Carlo model is developed. In this model, all atomistic reaction pathways in density functional theory (DFT) are implemented as reaction events on the lattice. This contains all steps, from the early stage of adsorption of each ALD precursor, kinetics of the surface protons, interaction between the remaining precursors (steric effect), influence of remaining fragments on adsorption sites (blocking), densification of each ALD precursor, migration of each ALD precursors, and cooperation between the remaining precursors to adsorb  $\text{H}_2\text{O}$  (cooperative effect). The essential chemistry of the ALD reactions depends on the local environment at the surface. The coordination number and a neighbor list are used to implement the dependencies. The validity and necessity of the proposed reac-

tion pathways are statistically established at the mesoscale. The formation of one monolayer of precursor fragments is shown at the end of the metal pulse. Adsorption and dissociation of the  $\text{H}_2\text{O}$  precursor onto that layer is described, leading to the delivery of oxygen and protons to the surface during the  $\text{H}_2\text{O}$  pulse. Through these processes, the remaining precursor fragments desorb from the surface, leaving the surface with bulk-like and OH-terminated  $\text{HfO}_2$ , ready for the next cycle. The migration of the low coordinated remaining precursor fragments is also proposed. This process introduces a slow reordering motion (crawling) at the mesoscale, leading to the smooth and conformal thin film that is characteristic of ALD. © 2013 Wiley Periodicals, Inc.

DOI: 10.1002/jcc.23491

## Introduction

Thin film materials, with thicknesses of the order of 1–100 nm, have a wide variety of technological applications. For their use in microelectronics, thin films must exhibit a high level of conformality, uniform stoichiometry, and controlled thickness. Atomic layer deposition (ALD) is an emerging low-temperature deposition technique providing relatively accurate control of composition and good conformality over high-aspect-ratio structures.<sup>[1,2]</sup> The films are capable of being used in nonplanar structures such as three-dimensional (3D) transistors. Use of thin film materials in the food packaging and pharmaceutical industry allow considerable savings in raw materials.<sup>[3]</sup> In addition, they can improve the humidity tolerance and performance of polymers. Developing new ALD processes require better understanding of how film growth depends on the chemicals being used.

ALD is a variant of chemical vapor deposition (CVD), in which two or more gaseous precursors are allowed to flow separately into a reactor in alternate pulses. Inert gas is admitted between each pulse to purge the remaining precursor from the reactor and avoid gas-phase reactions. Because of this, the precursors react with the substrate only. In the ideal case, ALD surface reactions are self-limiting, meaning that reactions cease after the formation of one monolayer of precursor fragments at the end of the pulse. Growth of the product film, therefore, takes place at the level of a submonolayer in each cycle, conformally coating all exposed surfaces if the dose in each pulse is sufficient.

The surface chemistry of ALD has not been fully investigated either experimentally or computationally, even for

popular systems such as  $\text{HfO}_2$  and  $\text{ZrO}_2$ . Different ALD precursors and processing conditions are observed experimentally to give different film properties<sup>[4]</sup> (e.g., morphology, conformality, thickness) and our assumption is that this is largely due to differences in the reaction pathways at the atomic scale accumulating over thousands of reaction events. A realistic ALD growth mechanism is extremely intricate and may consist of standard ALD acid/base reactions, structural relaxation, CVD-like reactions, and of influential factors such as steric hindrance, coreagent population, and the cooperative effects that we introduce in this article. The dependence of these mechanisms on temperature, the partial pressure of the precursor, pulse and purge times determines the measured process parameters such as ALD growth rate and film properties.

Modeling a complete ALD process requires integration of three modeling scales: a model for the reactive flow of the vapor-phase species on the scale of the whole reactor and within microscopic features,<sup>[5]</sup> a model for the evolution of the atomic structure at the growth surface, and a model for the reaction kinetics in both the vapor and at the surface. The overall ALD growth dynamics across all three scales is too complicated to be fully modeled. This article describes the

M. Shirazi S. D. Elliott

Tyndall National Institute, University College Cork, Lee Maltings, Cork, Ireland  
E-mail: [simon.elliott@tyndall.ie](mailto:simon.elliott@tyndall.ie)

Contract grant sponsor: Science Foundation Ireland (SFI) [Functional Oxides and Related Materials for Electronics (FORME), [www.tyndall.ie/forme](http://www.tyndall.ie/forme)]

© 2013 Wiley Periodicals, Inc.

reaction kinetics and structural relaxation at the growing surface, ignoring fluid dynamics and pressure fluctuations at either the feature or reactor scale. The information used in this model is obtained from an electronic structure model.<sup>[6]</sup> Before we describe our model in detail, we will briefly survey the existing literature on similar ALD models.

A simple analytical model, based on the mass balance of chemisorption, relates the growth rate to the size of the reactant and the chemisorption events.<sup>[7,8]</sup> Steric hindrance of the ligands controls the saturation of chemisorption at the adsorption sites. This model can be used for various ALD systems<sup>[9]</sup> if the mechanism is known. Although it can estimate growth rates, it does not give insights into the fundamental surface chemistry or predict properties such as the morphology of the film.

Another approach is to perform all-atom molecular dynamics (MD) simulations using an empirical interatomic potential. This technique has been used to model the growth of  $\text{Al}_2\text{O}_3$  from  $\text{Al}(\text{CH}_3)_3$  and  $\text{H}_2\text{O}$ .<sup>[10]</sup> Experimental results<sup>[11]</sup> show that ALD using this system is possible at low temperatures and, therefore, a relatively low activation energy for the gaseous by-product methane is expected. Hence, applying the interatomic potential for the amorphous alumina surface seems to be a well-suited approach to describing the structural relaxation during ALD growth. However, using MD simulation is unsuitable for ALD systems whose primary reactions fall into the category of the rare event.<sup>[12]</sup> Also, experimentally measured O/Al ratios vary between 1.34 and 1.70 depending on growth temperature.<sup>[11]</sup> In this situation, due to the process of densification, which is a driving force for the ALD reactions,<sup>[6]</sup> the Al atoms should exist at higher coordination number (c.n.) (i.e., c.n. = 5 or 6) than the calculated value (c.n. = 3 or 4). Therefore, a denser film than that actually obtained would be expected and the interatomic potential does not adequately describe the structural relaxation taking place during ALD growth.

Another approach is kinetic Monte-Carlo (KMC),<sup>[13]</sup> a powerful method for describing the stochastic time evolution of interdependent events. KMC is used in a wide range of areas from chemistry to biology. In KMC modeling, the true dynamical information (atomic positions and momenta) is dismissed and the atomic trajectories are replaced by a set of discrete positions, chosen from a set of predetermined possible atomic sites. KMC is ideally suited for modeling reaction events in surface science, involving adsorption, desorption, cooperative reaction, and structural relaxation at the surface of the growing film.<sup>[14,15]</sup> The method can reach simulation times of orders of magnitude longer than *ab initio* MD, while preserving a level of atomic detail. KMC can accommodate events at different time scales, including rare events. There are many KMC approaches, from coarse-grained model systems with hypothetical input values, to realistic atomic simulation with accurate chemical kinetics for the making and breaking of bonds. In the latter, a proper evaluation of surface kinetics at the mesoscopic scale is possible by using accurate information from first principles electronic-structure calculations.

Neizvestny et al.<sup>[16]</sup> used KMC as a coarse-grained model to simulate the ALD process. To reproduce the experimental

situation, hypothetical activation energies were used. However, the idea of KMC approach that we follow here is to carry the accuracy of electronic structure calculation theories to the mesoscopic scale. Along these lines a ground-breaking KMC model for ALD was proposed by Dkhissi et al.<sup>[17]</sup> that considered the ALD reactions and activation energies from density functional theory (DFT) calculations. They used a complicated lattice-based KMC to describe the growth of  $\text{HfO}_2$  from  $\text{HfCl}_4$  and  $\text{H}_2\text{O}$  on Si. A lattice framework was used to describe the transition between silicon crystal substrate and the oxide thin film. However, the complexity of the densification process on the growing surface was not implemented, insofar as changes in Hf and O c.n. from the gas to solid phase<sup>[6]</sup> and associated structural relaxation, was not considered. The steric demand of the precursor fragments was only partially accounted for.

As a general rule, an accurate description of a system by KMC requires a complete set of reaction pathways because the absence of an important reaction pathway results in a poor description. As will be shown in this study, the absence of cooperation between the remaining ligands to adsorb  $\text{H}_2\text{O}$  molecules<sup>[6]</sup> (which we term the cooperative effect) result in overestimation of the growth rate. In this study, multiple proton diffusion, steric effects, structural relaxation, and cooperative effects are included for the first time in ALD growth simulation and the necessity of including these in the meso-scale chemistry is justified.

Another major concern with the input data to the model is the accuracy of activation energies, which affects the growth rate and time evolution. The chemistry presented here has been obtained by *ab initio* calculations using DFT.<sup>[6]</sup> There is a systematic error due to the approximate DFT exchange-correlation functional that often results in underestimated activation energies for breaking and making bonds. This can in principle be overcome by using more accurate methods<sup>[18,19]</sup> rather than DFT. However, owing to the complicated reaction pathways that result from cooperative effects, computing large cells with many atoms (e.g., 500 atoms) is necessary, which is too computationally demanding for the more accurate methods. Hence, at the present time, we rely on the activation energies calculated using DFT. If all activation energies are underestimated, then the time taken to saturation during ALD will be too short, but the sequence of reactions will be correct.

The chemical reactions that can occur at a given site depend not only on the chemical identity of that site but also on the spatial environment—both local bonding to adjacent atoms (described via the c.n.) and steric effects due to more distant species. Hence, to implement the surface chemistry discussed earlier, a lattice-based KMC is used and the spatial environment is described through the c.n. and a neighbor list. Clearly, a lattice-based KMC does not explain the morphology of the film during ALD (e.g., crystalline vs. amorphous). In this study, we present only on-lattice KMC. However, the morphology of the film as a function of temperature could be studied by off-lattice KMC.<sup>[20]</sup> This means that the reported ALD reactions and their activation energies could be used for future off-lattice studies.

In the next section, some background of KMC simulations is described. However, the main part of this article is explaining how DFT-derived reaction pathways were implemented into lattice-KMC (Reaction Events section) and then evaluating how that played out as surface intermediates and growth behavior (Results and Discussion section).

## Computational Detail

### Transition-state theory

The common approach to modeling chemical kinetics is using transition-state theory (TST). In TST, the rate constant for the transition from a minimum A to a minimum B is estimated from the equilibrium flux crossing a dividing surface separating the two minima. The dividing surface is the hyperplane perpendicular to the reaction coordinate and the transition state (TS) is where the two intersect. Here, there are two assumptions. First, it is supposed that the system has reached thermal equilibrium between A and TS. Second, it is assumed that successful transitions through the dividing surface from A to B are uncorrelated, meaning that each forward transition through the dividing surface moves the system from A to B. For these assumptions to be valid, the best choice of dividing surface is near the saddle point in the minimum energy path between A and B, where the entire equilibrium flux is minimized. If thermal motion around the saddle point and the minima can be described by second-order expansions (harmonic vibrational modes) then the transition between the two minima can be explained by harmonic TST (hTST). From these assumptions, the rate constant  $k_{AB}$  for the transition from minimum A to minimum B can be derived from the Markovian state-to-state dynamics equation:

$$k_{AB}^{\text{TST}}(T) = A \exp(E_a/k_B T) \quad (1)$$

where  $E_a$  is activation energy and the prefactor is determined from

$$A = f_{AB}^{\text{TST}}(T) (k_B T / h) \quad (2)$$

where  $h$  is Planck's constant,  $k_B$  is the Boltzmann constant,  $T$  is temperature and where

$$f_{AB}^{\text{TST}}(T) = (q_{\text{TS}}^{\text{vib}} / q_A^{\text{vib}}) \quad (3)$$

where  $q_{\text{TS}}^{\text{vib}}$  and  $q_A^{\text{vib}}$  are the vibrational partition functions at the TS and at the bound state A, respectively.

Thus, to evaluate  $k_{AB}^{\text{TST}}$ , static information about the potential energy surface (PES) at the initial minimum A and at the TS and the partition functions at those locations are typically required. In most cases involving surface-bound reactants and products, the vibrational properties of the system at the minimum and TS are found to be similar. Internal rotational components of species at the surface have a tiny influence on the vibrational partition function. This inaccuracy in prefactor is negligible in comparison with inaccuracy of activation energy in exponential factor. Hence, we consider the ratio  $f_{AB}^{\text{TST}}(T) \sim 1$ ,

eq. (3). However, gas-surface reactions include large changes in entropy and so this assumption does not apply. The prefactor has values of the order of  $10^{12}$ – $10^{13} \text{ s}^{-1}$  depending on temperature. In hTST, the key information from the PES which is entered into eq. (1) is  $E_a$ , the potential energy of the TS relative to the (meta)stable initial minimum. In ALD, many TSs correspond to situations where bonds are made or broken.  $E_a$  for such situations can be obtained from *ab initio* quantum chemistry models. These models, in the Born–Oppenheimer presentation, treat electrons adiabatically at every configuration of atomic positions and atomic dynamics take place on the resulting PES.

However, hTST certainly cannot be used for the adsorption process ( $A = \text{gas-phase}$ ,  $B = \text{adsorbate on surface}$ ). Adsorption of the precursor takes place with a probability given by Maxwell–Boltzmann statistics. The molecular flux or impingement rate to the adsorption sites is obtained from

$$k_{n,B}^{\text{ads}}(T, P_n) = \frac{S_{n,B}(T) P_n A_{\text{uc}}}{\sqrt{2\pi m_n k_B T}} \quad (4)$$

where  $S_{n,B}(T)$  is the sticking coefficient that quantifies the fraction of molecules that stick to an adsorption site (for simplicity, it was assumed that  $S_{n,B} = 1$ ).  $P_n$  and  $m_n$  are the partial pressure and the mass of precursor molecules, respectively.  $A_{\text{uc}}$  is the area of the surface unit-cell including site B and  $n$  is a label for different precursor.<sup>[15,21]</sup> In this study, the desorption rates are described using eq. (1), because the activation energies for desorption can be calculated by the nudged elastic band (NEB) method.

### Time evolution

A KMC simulation consists of a sequence of separate hops from one minimum to another (known as “events”) taking place at sites within the simulation cell. The random choice of which event at which location after which amount of time is governed by KMC. Starting from a given minimum, the KMC algorithm determines which minimum to hop to and the appropriate time step  $\Delta t$ , therefore, changes at each KMC iteration. The system clock is advanced by this time:

$$t = t + \Delta t \quad (5)$$

Each pathway, therefore, has its own probability (Poisson) distribution function for time evolution. The probability of event  $m$  consisting of hopping from minimum  $i$  to minimum  $j$  at a given site is given by eq. (6):

$$p_m(\Delta t) = k_{ij} \exp(-k_{ij} \Delta t) \quad (6)$$

The system has many possible events each with a fixed probability that is obtained its rate constant  $k_{ij}$  using eq. (1). To advance the dynamics of the system in time, many numerical KMC algorithms have been suggested in the literature.<sup>[13]</sup> The first-reaction method<sup>[22]</sup> uses eq. (7) to determine the timestep for each possible event.

$$\Delta t_m = \frac{\ln(\rho_m)}{k_m} \quad (7)$$

where  $m = 1, \dots, N$ . This algorithm has been used for ALD modeling.<sup>[17,23]</sup>

A random number  $\rho_m \in [0, 1]$  for each of the  $N$  possible events is generated, so that the timesteps are properly weighted by the rate constants. The pathway with the shortest timestep is chosen and executed. The system moves to the new state (minimum), and the system clock is advanced by the corresponding shortest timestep. In this algorithm, many random numbers must be generated, all of which are discarded apart from one.

Another commonly used algorithm was proposed by Bortz, Kalos and Lebowitz (BKL)<sup>[24]</sup> and is also referred as the Gillespie,  $N$ -fold way, or residence-time algorithm. Initially, the BKL algorithm as with any KMC algorithm, begins by finding all  $N$  possible pathways across all the sites in the simulation cell. The corresponding  $N$  different rate constants are obtained using eq. (1). The algorithm accumulates all the possible events together with their associated rates into an event list. Then, the total rate constant is obtained by summing all the individual rate constants:

$$k_{\text{tot}} = \sum_{m=1}^N k_m \quad (8)$$

Then, in contrast to the first-reaction method, only two random numbers  $\rho_1$  and  $\rho_2 \in [0, 1]$  are generated. When  $N$  is large, generating and processing two random numbers instead of  $N$  random numbers makes a large computational difference. Hence, the first-reaction method is not as computationally efficient as the BKL method.  $\rho_1$  is used to select one of the possible events via eq. (9). Obviously, an event with a large rate constant is more likely to occur. Therefore, the algorithm searches for the event  $q$  in the event list that fulfills eq. (9) and the event  $q$  is executed.

$$\sum_{i=1}^{q-1} k_i \leq \rho_1 k_{\text{tot}} \leq \sum_{i=1}^q k_i \quad (9)$$

An update of the event list is needed after each execution of an event. Even if the system includes thousands of potential events, typically only a few events are removed and a few events are added (in the order of 1–10) to the event list after each execution. It is most efficient to preserve the event list and simply modify the executed event and affected events in the vicinity of that site. Therefore, reinitialization of all possible events in each iteration is not required, an enormous computational saving. In fact, updates of the event list have a much higher impact on the computational cost than generating the random numbers. In this respect, the first reaction method and BKL algorithm perform similarly well.

The other important aspect of the BKL algorithm is the time step and how the system clock is advanced. By executing the chosen event, the system moves to the new state and the system clock is advanced by the equation below:

$$t = t - \frac{\ln(\rho_2)}{k_{\text{tot}}} \quad (10)$$

where  $\rho_2$  is the second random number. The time evolution is independent of the chosen event, but does depend on the total sum  $k_{\text{tot}}$ . This means that when high rate events (fast processes) become dominant—not only in terms of weight but also in terms of number—the simulation advances extremely slowly. Such disparity between low and high rate events occurs when the system is trapped in a set of adjacent minima (a “superbasin”). In this situation, a more advanced model<sup>[25]</sup> is needed that reduces the occurrence of frequent events. Our KMC model is also faced with the problem of this disparity (see subsection Proton diffusion).

Some of the events observed during *ab initio* MD are highly exothermic and barrierless or have a small barrier (less than 0.2 eV) and so may be thought of as deterministic, rather than stochastic. To implement these processes in the stochastic model, a small barrier (0.2 eV) is assigned to each of the deterministic processes. The definition of a small barrier can be problematic because it can create a disparity in the rate of reactions and disturb the time evolution of the system. However, the reverse of these deterministic process is extremely rare and, therefore, the reverse reaction is omitted from our event list.

A larger system typically means more events. More events in the total event list means that the sum  $k_{\text{tot}}$  in the BKL approach becomes larger, even though the same reaction list is used. Hence, the system clock progresses slower for a large system than for small one, which is physically correct. However, to achieve a realistic cycle time for an ALD process with a reasonable computational time, some fast processes are ignored.

The system size and the fast processes, therefore, largely dictate the progress of the simulation time. In order to tackle a realistic ALD system, many reactions have to be included (see Reaction Events section).

### KMC solver

The ALD application was developed as a new feature in the stochastic parallel particle kinetic simulator (SPPARKS)<sup>[26,27]</sup> code. SPPARKS is written in a modular fashion, allowing new functionality to be added in a straightforward manner. All possible events are specified before the simulation begins. The event list consists of all possible events at each site. Rejection KMC is chosen as the KMC solver for choosing an event from the event list. This KMC solver uses the previously defined BKL-algorithm<sup>[24]</sup> to update the system clock by eq. (10). The solver executes the chosen event and modifies the occupation of sites. The event list is updated by removing events that have become invalid at modified sites and adding new events for these sites to the event list.

### Lattice site

To track the surface evolution and film morphology, a lattice-based KMC method is used. The lattice can in principle be two



dimensional (2D) or 3D. Tracking in three dimensions is much more difficult than in two dimensions due to the far greater topological complexity. However, to accurately translate the chemistry in the atomic scale to the mesoscale for ALD, 3D tracking is deemed necessary. The capability to describe the system in 3D makes modern KMC a powerful tool to explain both reaction kinetics and film morphology. The two precursors considered in this study are  $\text{Hf}(\text{N}(\text{CH}_3)_2)_4$  and  $\text{H}_2\text{O}$ . In this article, the ligand  $\text{N}(\text{CH}_3)_2$  is referred to as X for simplicity.

The lattice sites are defined based on monoclinic  $\text{HfO}_2$  (space group  $\text{P}2_1/\text{c}$ )<sup>[28]</sup> as this is the most stable crystalline structure of the oxide after deposition and annealing. The 3D lattice sites are occupied by either Hf or O atoms during the ALD simulation. In the monoclinic structure, every site of the cation sublattice is surrounded by seven anion sites and every site of the anion sublattice is surrounded by three or four cation sites (Fig. 1). Based on the counted number of first neighbor atoms of a cation or anion, the c.n. was defined. Every cation or anion site can have a c.n. ranging from 0 up to 7 or 4, respectively. We exclude bonds to H when quoting the c.n. of O.

The crystallographic directions  $\langle 111 \rangle$  define the x,y, and z axes of the coordinate system. Periodicity is imposed in x and y but not in z. Two smooth layers of fixed oxygen and hydroxyl in the x-y plane are considered as the substrate in this example. The first cycle starts with a  $\text{HfX}_4$  pulse. The crystal growth is then in the +z direction. Each lattice site is associated with three variables describing the state of this site.

- The first variable contains the information regarding the chemical identity of the site. This variable is updated frequently during the KMC simulation.

- Each lattice site also has a neighbor list that carries the information about the local bonding. Local bonding indicates which site is connected to which site and this assists in

defining the reaction events in KMC. Structural relaxation, cooperative reactions, and steric hindrance are implemented using the neighbor list.

- Finally, each lattice site is associated with a discrete variable describing the c.n. of the site. This variable, together with the neighbor list, allows us to implement the complicated chemistry at the surface. For instance, by densification of the hafnium atom of the precursor to the surface, the c.n. of a cation site can change from 0 to a limit of 3–8.

### Pulse time and purge time

In the ALD process, gaseous precursors are admitted to the reactor in alternate pulses separated by periods of purging. To implement this in KMC, the respective adsorption reactions are turned on and off as simulation time advances. Adsorption reactions occur alternately as time progresses.

## Reaction Events

### Event type

In our KMC model, reaction events are defined and used to implement the chemistry of ALD obtained from DFT calculations.<sup>[6]</sup> For every position, geometry optimization was carried out by DFT calculations. The minima obtained from the DFT calculations are mapped onto the lattice sites for the subsequent KMC calculations. The events taking place within the KMC calculation modify the chemical occupation of the sites. This corresponds to the transition of the system from one minimum to another in the DFT calculation. The frequency of an event is derived using eq. (1) from an activation energy obtained from NEB<sup>[29]</sup> calculation with DFT.

We consider that three types of events occur, each with different dependencies on neighbors. Here, the site under

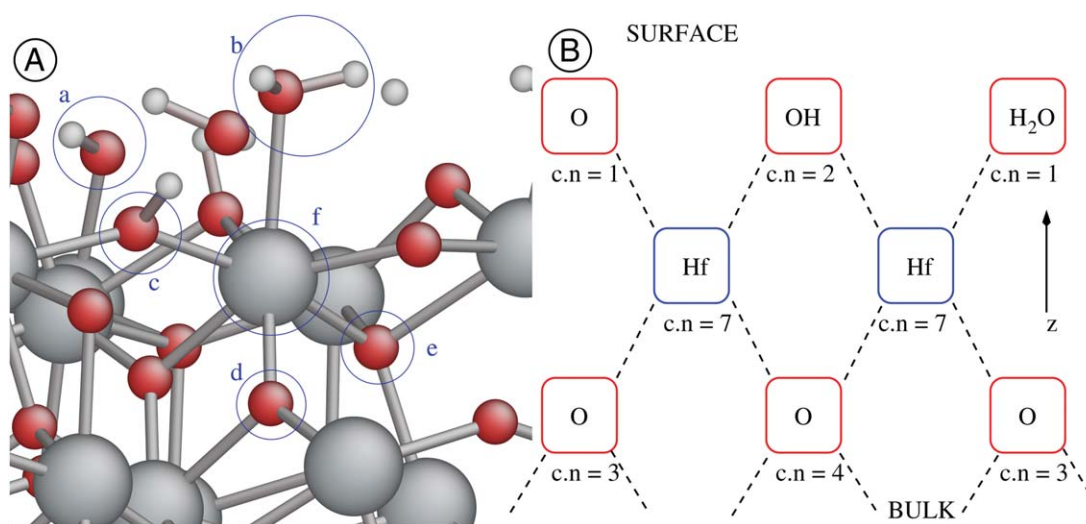


**Figure 1.** (A) DFT optimized surface structure of hydroxylated  $\text{HfO}_2$ .<sup>[6]</sup> Terminal hydroxyl group (a), terminal adsorbed water (b), bridging hydroxyl (c), three coordinated oxygen (d), four coordinated oxygen (e), and seven coordinated hafnium (f) are highlighted. (Red = O, White = H, large grey = Hf). (B) Schematic 2D diagram illustrating mapping of the same surface structure. Blue and red boxes show the cation and anion sites, respectively. The dashed lines show the connection between sites in this 2D diagram but the actual c.n. in three dimensions is also given.

consideration is specified by  $\square^{(0)}$ . The first and second neighbors of the involved site are identified by  $\square^{(1)}$  and  $\square^{(2)}$ , respectively. The occupation of the first or second neighbor site may also change as a result of an event at  $\square^{(0)}$ .

**Type  $\alpha$ .** This type of event only changes the occupation of a single site. The event is dependent on the c.n. at that site and on the pulse/purge stage of the ALD cycle. For instance,  $\text{OH}^{(0)} \rightarrow \text{OH-HfX}_4^{(0)}$  only occurs for the hydroxyl group with a c.n. of oxygen = 1 (excluding H) during the hafnium precursor pulse. The possibility of adsorption, therefore, is limited to the anion site with OH occupation during the metal pulse.

**Type  $\beta$ .** This event modifies the occupation of a site  $\square^{(0)}$  and the second neighbor of this site  $\square^{(2)}$ . Clearly, the possibility of this event occurring depends on the characteristics of the site and on those of its second neighbor. As with type  $\alpha$ , events, there can be a dependence on the c.n. and on the pulse/purge stage of the ALD cycle. For example, consider an adsorbate site as an anion site occupied with adsorbed  $\text{HfX}_4$ , whose first and second neighbors are cation and anion sites, respectively. Then, the event  $[\text{OH-HfX}_4]^{(0)} + \text{OH}^{(2)} \rightarrow [\text{OH-Hf(HX)X}_3]^{(0)} + \text{O}^{(2)}$  only occurs when there is a proton  $\text{OH}^{(2)}$  in the second neighbor of the adsorbate site.

**Type  $\gamma$ .** This event type changes the occupation of a site and of its first neighbor. For instance,  $[\text{OH-HfX}_2]^{(0)} + \text{VAC}^{(1)} \rightarrow \text{OH}^{(0)} + \text{HfX}_2^{(1)}$  shows the motion of a hafnium precursor fragment to an adjacent vacant cation site. In this case, the event changes the occupation of the adsorbate site  $\square^{(0)}$  (anion sublattice) and the vacancy site  $\square^{(1)}$  (cation sublattice). Following an event of this type, the c.n.'s of both adsorbate and vacancy sites must be updated.

In the following discussion, the atomic-scale chemistry of the surface determined<sup>[6]</sup> from DFT is translated into discrete events in order to describe the KMC simulation in more detail.

### Hf precursor adsorption

Molecular  $\text{HfX}_4$  chemisorption takes place with a probability given by eq. (4). There are three criteria that adsorption sites of  $\text{HfX}_4$  must satisfy as outlined below.

- First, DFT calculations<sup>[6]</sup> have shown that the adsorption sites are singly coordinated oxygen and hydroxyl groups ( $\square^{(0)} = \text{O}$  or  $\text{OH}$  with c.n. = 1). In other words, the bridging oxygen and crystalline oxygen with c.n. > 1 are unsuitable for adsorption.

- Second, the adsorption sites can be blocked due to the remaining X at neighboring sites. There are different rules for remaining ligands of  $\text{HfX}_4$ ,  $\text{HfX}_3$ ,  $\text{HfX}_2$ , and  $\text{HfX}$  as discussed in subsection Steric effect.

- Third, the adsorption sites can be blocked due to O at neighboring sites. As anion sites are occupied by oxygen during the oxygen pulse, low coordinated O or OH (c.n. = 1) in the sublayers become inaccessible to the precursor metal. To prevent the adsorption at these sites, the number of oxygen atoms occupying second neighbors of the relevant oxygen site are counted. If this number is greater than 4/5 of the total

sites, then the relevant site is blocked. This process only happens during the Hf pulse.

If all sites are occupied or blocked, the incident hafnium precursors are assumed to be reflected back to the gas phase.

### $\text{HfX}_4$ desorption

The reverse of  $\text{HfX}_4$  adsorption is desorption. As with adsorption, the desorption event is of type  $\alpha$ . Neighboring sites are unblocked via desorption of  $\text{HfX}_4$ . In our KMC calculation, desorption of charged precursor fragments like  $[\text{HfX}_3]^+$  or intermediates like  $[\text{Hf(HX)X}_3]^+$  is not allowed.

### Proton diffusion

In our KMC model, various types of proton diffusion are defined. There is a strong correlation between these diffusion events and other reactions. For example, the ready availability of protons contributes to the facile elimination of ligands. Increased eliminations during the metal pulse lead to a higher rate of growth.<sup>[30]</sup> As one of the aims of this model is to judge exactly how the rate of growth is affected by these diffusion events, they are sorted into four types below.

#### – Proton diffusion from oxygen to oxygen

Proton diffusion from oxygen to oxygen is the reaction that allows mobility of protons across the surface. The c.n. of oxygen (at an anion site) is used to distinguish between the proton diffusion barriers. DFT calculations show that it is energetically favorable for protons to move from high c.n. oxygen to low c.n. oxygen. Hence, under-coordinated oxygen (with c.n. = 1 or 2) are the Brønsted basic sites that are actively involved in proton diffusion. A one coordinated oxygen is a hyperactive site. It spontaneously decomposes a neighboring  $\text{H}_2\text{O}$  molecule (type  $\beta$ ) or takes a proton from a higher coordinated oxygen (c.n.  $\geq 2$ ). According to DFT calculations, both of these reactions are barrierless. A two coordinated oxygen is less active than a one coordinated oxygen. The two coordinated oxygen faces a large barrier to taking a proton from a neighboring oxygen (c.n. = 1). After depletion of protons at the surface due to desorption as HX, some oxygen atoms acquire a higher c.n. due to densification, whereas the other oxygen atoms acquire a reduced c.n. and become more Brønsted basic. These latter under-coordinated oxygen undergo a form of proton diffusion from oxygen to oxygen with the same c.n. A 0.75-eV barrier for these one or two coordinated oxygen atoms is obtained by DFT.

#### – Proton diffusion from oxygen to ligand nitrogen (from anion to anion site)

The other type of proton diffusion is from the surface oxygen to the nitrogen of the precursor and its reverse. In the case of alkylamide,<sup>[6]</sup> it has been shown that there are stable geometries with a proton bound to the nitrogen. The formation of HX in this manner is necessary prior to ligand

elimination by desorption of HX. However, the activation energy strongly depends on the distance between N and O. If we suppose that  $\text{HfX}_4^{(0)}$  is anchored to an  $\text{OH}^{(0)}$  group at the surface (type  $\alpha$ ), the most accessible proton for hopping to the  $\text{N}^{(0)}$  of the precursor is not the anchor  $\text{OH}^{(0)}$ , but rather the second neighbor protons ( $\text{OH}^{(2)}$ ), because the  $\text{N}^{(0)}\text{-O}^{(2)}$  distance is shorter. The activation energies for proton diffusion from the surface oxygen to the nitrogen of the ligand and its reverse range from 0.05 to 0.30 eV. To map this proton hopping behavior into KMC, type  $\beta$  events are introduced that change the occupation of the site and its second neighbor.

In comparison to the barrier to rotation for the protonated ligand discussed in subsection Rotation of the protonated ligand, diffusion of the proton from nitrogen back to the oxygen has a lower barrier. This means that proton diffusion between the surface oxygen and the nitrogen and its reverse is much faster than rotation of the protonated ligand. The most likely events which occur are low barrier events. Hence, the KMC simulation advances extremely slowly, especially considering that the sum of probabilities is over a large number of sites, giving a total rate that is enormously large (superbasin) (subsection Time evolution). To overcome this difficulty, we propose that only the presence of a proton on surface oxygen is necessary for protonation and rotation of the ligand. In other words, we remove (filter) proton diffusion from the surface oxygen to the nitrogen and its reverse from the reaction list. Otherwise, the realistic ALD time will be inaccessible to the current KMC simulation. A side-effect of this is that time evolution of the system does not correspond to the realistic ALD time.

- Proton diffusion from oxygen to nitrogen (from anion to cation site)

This diffusion describes proton hopping from oxygen ( $\square^{(0)}$ ) to the first neighbour nitrogen of the densified precursor ( $\square^{(1)}$ ) which is explained in subsection Densification of  $\text{HfX}_2$ . This diffusion occurs from the anion site to the cation site (type  $\gamma$ ).

- Proton diffusion from nitrogen to nitrogen

Proton diffusion within the adsorbed precursor consists of proton hopping from nitrogen near the surface to the top-most nitrogen of the precursor. This diffusion is of type  $\alpha$ .

In this calculation, no particular ligand orientation for proton diffusion is considered.

### Rotation of the protonated ligand

After diffusion of a proton from the surface oxygen to the ligand nitrogen, there is a second reaction that facilitates elimination of HX, namely rotation of the protonated ligand. Activation energies of 0.42–0.51 eV are calculated for the rotation of alkylamide ligand.<sup>[6]</sup> To implement this reaction in combination with proton diffusion from the surface oxygen to the nitrogen, event type  $\beta$  is used.

### Elimination of the ligand

It is commonly assumed that protonated ligands (HX) rapidly desorb following proton transfer from the surface to the remaining fragment during ALD. However, we have shown<sup>[6]</sup> that further proton transfer to the remaining fragment before desorption facilitates the ligand elimination. For instance, the activation energy for desorption of the first HX after the first protonation and rotation is 0.89 eV. This energy decreases to 0.39 eV after the second protonation. A third protonation allows spontaneous desorption ( $E_a = 0$  eV) of two HX and densification of the metal precursor. In order to map the desorption of HX into the KMC model, the occupation of a single site is modified (type  $\alpha$ ). Neighboring sites have no direct influence on the desorption event. The last HX desorption from the Hf precursor is an endothermic reaction. Such an event takes place only if either of the following occurs:

- The Hf of the precursor is densified into an empty cation site surrounded by least six oxygen atoms; conversely, an empty site in the subsurface layer.
- The c.n. of Hf of the precursor is increased by adsorption of  $\text{H}_2\text{O}$  during the oxygen pulse, as explained later.

### Densification of $\text{HfX}_2$

*Ab initio* MD calculations<sup>[6]</sup> show that after elimination of two ligands from the adsorbed  $\text{HfX}_4$ , the Hf atom of the remaining  $\text{HfX}_2$  fragment becomes strongly bonded to nearby under-coordinated oxygen at the surface. This structural relaxation is termed “densification” and is implemented in the KMC model as event type  $\gamma$  with a small barrier (0.2 eV). The  $\text{O-HfX}_2^{(0)}$  remnant moves from the anion site where it was adsorbed to one of the neighboring cation sites  $\square^{(1)}$  where the Hf belongs (Fig. 2). To implement densification in the KMC simulation, the c.n. of the anion and cation sites involved in densification are modified. As mentioned above, every site  $\square^{(0)}$  of the anion sublattice is connected to 2 or 3 cation sites  $\square^{(1)}$  at the surface. To determine which cation site is chosen, a random procedure is used, which is not strictly correct. The correct dependence on c.n. is included via the migration process (see subsection Migration of  $\text{HfX}_2$ ).

Typically hafnium, together with the remaining fragments, forms three or four bonds to the smooth surface following densification (Fig. 7). In this case, densification is highly exothermic ( $\Delta G \leq -4$  eV) and an enormous activation energy is needed for the reverse reaction. Also, densification into the sublayers (filling gaps in a rough surface) is expected to be even more exothermic than on a smooth surface. This means that a huge amount of energy is needed to detach the hafnium (with the remaining precursor) from three or four oxygen atoms, which is not possible energetically in the ALD process. Hence, the reversal of densification is neglected in our calculation.

The hafnium should finally become densified to the cation site that has highest c.n. to surface oxygen. In other words, stronger attraction from higher number of Brønsted base sites

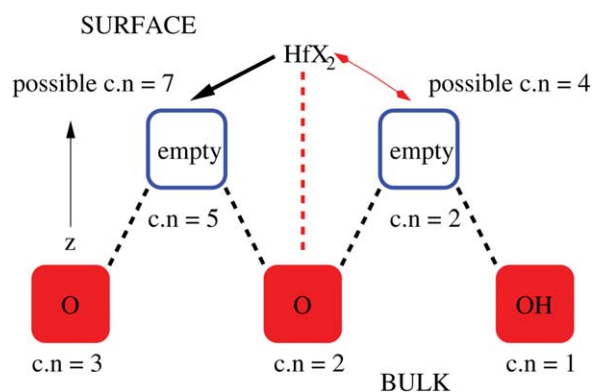


**Figure 2.** Schematic diagram of densification of  $\text{HfX}_2$  into empty cation sites. The presence of more under-coordinated oxygen around the left-hand cation site applies speculatively a stronger attractive force on the  $\text{HfX}_2$  adsorbate than that at the right-hand site. The thicker black arrow indicates the stronger attraction where reverse densification is impossible. Red arrows show migration process. (Same scheme as Fig. 1). [Color figure can be viewed in the online issue, which is available at [wileyonlinelibrary.com](http://www.interscience.wiley.com).]

is hypothetically applied to the hafnium than less one. For instance, in Figure 2, the five-coordinated empty site exerts a stronger attraction to the hafnium than the empty two-coordinated site. Therefore, the hafnium of the precursor should densify to the cation site with a higher c.n. rather than moving randomly. This tendency will be included using the migration process (subsection Migration of HfX<sub>3</sub>).

### Migration of $\text{HfX}_2$

In our KMC model, densification happens all over the surface. It may happen into the sublayer, in which case a high c.n. for Hf to previously under-coordinated oxygen is obtained, or it may happen by reorganization of bonding at the smooth surface, typically leading to a Hf c.n. of 3 or 4 from the under-coordinated oxygen. In the cases discussed earlier, hafnium with its remaining ligands has a total c.n. of 5 at least. However, densification may also happen when there is a low population of surface oxygen (Fig. 3). In this case, the hafnium is not coordinatively saturated. For instance, if  $\text{HfX}_2$  contains two bonds due to the bonding to the surface oxygen, it has total c.n. of 4. In this situation, DFT calculations show that the hafnium of the precursor keeps its two ligands and no HX

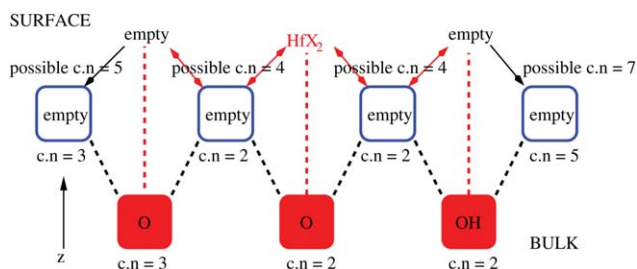


**Figure 3.** Schematic diagram of densification and migration of  $\text{HfO}_2$  (Same scheme as Fig. 1). Black arrows show potential densification where reverse densification is impossible. Red arrows show migration process. The migration process occurs until a c.n. greater than 2 is obtained by hafnium of the precursor. [Color figure can be viewed in the online issue, which is available at [wileyonlinelibrary.com](http://www.interscience.wiley.com).]

desorption has been seen, as the activation energy is high. The mobility of this four-coordinated  $\text{HfX}_2$  has been seen during *ab initio* MD.<sup>[6]</sup>

The migration process is only defined for three- or four-coordinated  $\text{HfX}_2$  ( $E_a = 0.40$  and  $0.50$  eV, respectively). In this picture, a  $\text{HfX}_2^{(0)}$  fragment that has migrated to a cation site, can come back to an oxygen atom  $\text{O}^{(1)}$  at an anion site. The reverse can also take place ( $\text{O-HfX}_2^{(0)}$  anion site to  $\square^{(1)}$  cation site) as shown in Figure 3. In this situation, migration events continue until the metal of the precursor becomes five or more coordinated in total. For instance, if  $\text{HfX}_2$  does densify into possible sites with c.n. = 5 or 7 (Fig. 3), the hafnium atom remains pinned at this cation site. No reverse migration is then possible any more. In this manner, any concerns regarding the occurrence of random densification in the low coordinated cation site are addressed.

The migration combined processes of random densification and introduce a slow motion of Hf fragments over the low coordinated anion sites of the oxygen-covered surface. We call this motion “crawling.” The precursor fragment crawls over areas with a low population of surface oxygen until the hafnium of the precursor finds a site that is abundant in oxygen and thus obtains a high enough c.n. from the surface oxygen. This mechanism allows subsurface vacancies to be filled. Our tests show that this mechanism has a profound effect on film growth in KMC.

### Steric effect

The metal cation in the precursor molecule is surrounded by ligands that are often large, as in the current case of  $X = N(CH_3)_2$ . These ligands take up substantial space at the surface when the precursor molecule or its fragments are adsorbed. Many potential adsorption sites around such a fragment, therefore, lose their capability to adsorb further precursors. This steric effect is obviously an important consideration, which affects the rate of ALD growth and the statistics of the different configurations in the KMC calculation. To model the interactions between the remaining fragments of the precursors, and their secondary influence on the adsorption sites, DFT calculations are used. Figure 4 shows the optimized structure of two neighboring  $HfX_3$  precursors at the surface, where both are anchored to under-coordinated oxygen at the surface. The distance between the hafnium atoms of the fragments is 8.4 Å. Optimizing the geometry from other adsorption sites for  $HfX_3$ , no shorter Hf-Hf distance could be obtained, so this may be viewed as a minimum value. The sites where closer approach was impossible (the highlighted oxygen atoms in Fig. 4) have, therefore, temporarily lost their ability to adsorb another precursor molecule. We term this process “blocking.”

To implement this blocking at the surface, the neighbor list of the site is used. Following adsorption of  $\text{HfX}_4$  at the  $\text{OH}^{(0)}$  (c.n. = 1) site, the relevant neighboring anion sites (the second neighbors  $\square^{(2)}$  and fourth neighbors  $\square^{(4)}$ ) are flagged as blocked and drop out from the reaction list for adsorption (Fig. 5). Similar blocking of  $\square^{(2)}$  and  $\square^{(4)}$  is also applied when fragments of precursors remain, namely  $\text{HfX}_3^{(0)}$  and  $\text{HfX}_2^{(0)}$



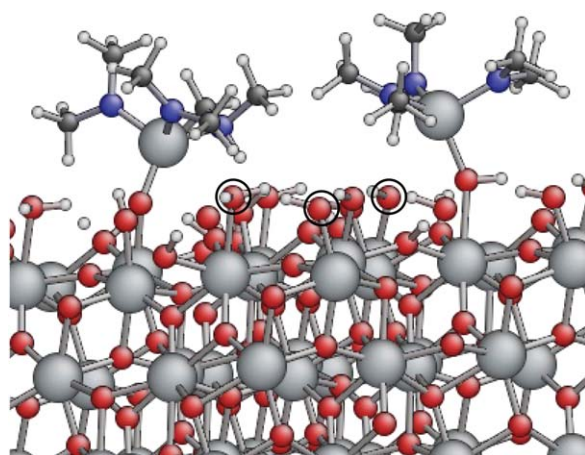


**Figure 4.** Steric hindrance between two  $\text{HfX}_3$  from DFT calculation. Steric hindrance leads to a change in the adsorption pattern of the precursors in ALD. Some of the blocked sites are highlighted indicating that they are unable to adsorb the next Hf precursor. (Red = O, White = H, large grey = Hf, dark grey = C, and blue = N). [Color figure can be viewed in the online issue, which is available at [wileyonlinelibrary.com](http://wileyonlinelibrary.com).]

before densification. Implementation of blocking after densification is slightly different, as now  $\text{HfX}_2^{(0)}$  is on a cation site. The neighboring anion sites that it blocks are  $\square^{(1)}$  and  $\square^{(3)}$  (see Fig. 6).

The other potential steric effect is the blocking of Hf fragments from densifying at a cation sites, due to the existence of fragments at adjacent sites. When hafnium, together with the remaining ligands, is densified to a cation site  $\square^{(0)}$ , it might prevent further densification in the neighboring cation sites  $\square^{(2)}$ . However, DFT calculations show that densification of such fragments to adjacent cation sites is possible. Figure 7 shows three neighboring  $\text{HfX}_2$  in which ligands are aligned to each other. The distance between Hf-Hf in the  $\text{HfX}_2$  is slightly stretched to minimize repulsion between the remaining fragments. Applying the blocking process to the adjacent anion sites ensures that there is enough surface area available for these fragments.

DFT calculations show that as many  $\text{HfX}$  as possible can be densified into the adjacent cation positions. In Figure 8, four  $\text{HfX}$  are densified into adjacent cation positions. The typical

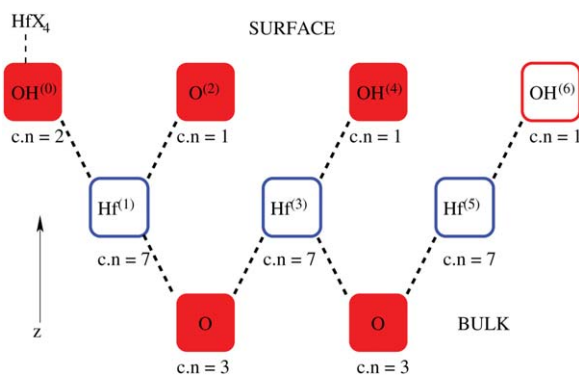


**Figure 5.** Schematic 2D diagram of blocking after adsorption of the undensified hafnium precursor. The filled boxes show blocked sites with respect to further adsorption of  $\text{HfX}_4$  due to the presence of  $\text{HfX}_4$  adsorbate at the surface site on the left (Same scheme as Fig. 1). [Color figure can be viewed in the online issue, which is available at [wileyonlinelibrary.com](http://wileyonlinelibrary.com).]

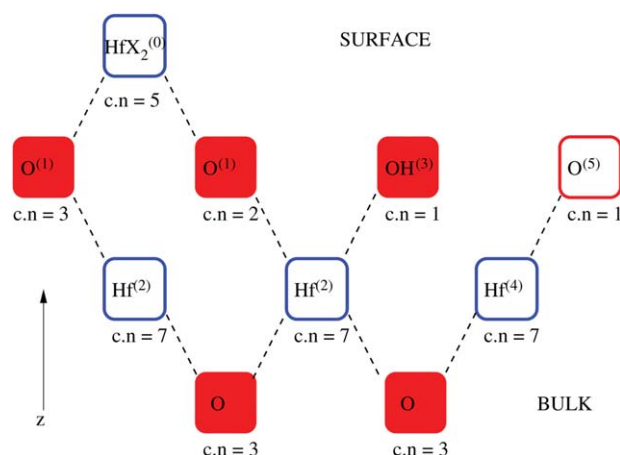


**Figure 6.** Schematic diagram of blocking after densification of the hafnium precursor onto a cation site. The presence of  $\text{HfX}_2$  at the cation site precludes adsorption (filled boxes) at fewer sites than in  $\text{HfX}_4$  at an anion site (Fig. 5). [Color figure can be viewed in the online issue, which is available at [wileyonlinelibrary.com](http://wileyonlinelibrary.com).]

minimum distance between Hf-Hf in bulk  $\text{HfO}_2$  is 3.3 Å. In Figure 8, the distance between the highlighted Hf in the cluster is also 3.3 Å. This means that the repulsion between the remaining ligands declines in a surface covered with  $\text{HfX}$  when compared to  $\text{HfX}_2$ . The presence of  $\text{HfX}$  does not prevent adsorption at next neighboring anion sites  $\square^{(3)}$ . Therefore, following desorption of  $\text{HX}$  from  $\text{HfX}_2$  to leave  $\text{HfX}$ , blocking is lifted from all the surrounding anion sites.

## H<sub>2</sub>O adsorption

The probability of  $\text{H}_2\text{O}$  adsorption from the gas phase, like  $\text{HfX}_4$  adsorption, is described by Maxwell-Boltzmann statistics [eq. (4)]. In DFT simulations, we find that adsorption of Lewis basic  $\text{H}_2\text{O}$  takes place at specific sites of sufficient Lewis acidity, namely Hf atoms that are not coordinatively saturated. For instance, the X fragments in adsorbed  $\text{HfX}_3$  push  $\text{H}_2\text{O}$  away

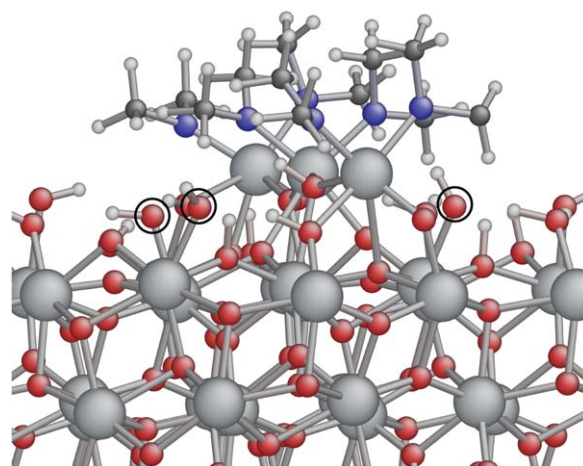


**Figure 7.** A cluster of three  $\text{HfX}_2$  in adjacent cation/cation sites (DFT). The highlighted oxygen atoms are some of those that are blocked with respect to adsorption of another hafnium precursor. The Hf-Hf distance is stretched (3.9 Å) to minimize repulsion between the aligned ligands. [Color figure can be viewed in the online issue, which is available at [wileyonlinelibrary.com](http://wileyonlinelibrary.com).]

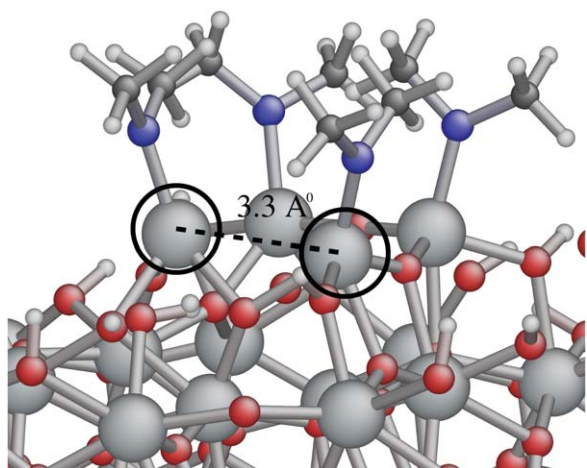


**Figure 8.** A cluster of four HfX in adjacent cation/anion sites (DFT). The distance between highlighted hafnium atoms (3.3 Å) shows that repulsion between the aligned ligands is less problematic than in the case depicted in Figure 7. [Color figure can be viewed in the online issue, which is available at [wileyonlinelibrary.com](http://wileyonlinelibrary.com).]

from Hf and prevent bonding of the water molecule. Results from *ab initio* MD and DFT calculations show that adsorption of a H<sub>2</sub>O molecule to an existing HfX occurs, provided that another HfX exists as a second neighbor of this HfX site, a so-called “cooperative” reaction.<sup>[6]</sup> Therefore, adsorption of H<sub>2</sub>O occurs at a pair of HfX or low coordinated Hf. The H<sub>2</sub>O molecule is initially bridging between under-coordinated (Fig. 9) hafnium, and is then decomposed by the neighboring oxygen or nitrogen into H + OH. The adsorption of H<sub>2</sub>O is, therefore, a type  $\beta$  event. There is no steric blocking of adjacent sites by adsorbed H<sub>2</sub>O.

### H<sub>2</sub>O densification and ligand exchange

Possible H<sub>2</sub>O adsorptions at the HfX–H<sub>2</sub>O<sup>(0)</sup> (cation site) clusters are followed by densification of the H<sub>2</sub>O molecule on to the  $\square^{(1)}$  anion sublattice so that oxygen becomes coordinated to a greater number of neighboring Hf. Similar to HfX<sub>2</sub>, densification of a H<sub>2</sub>O molecule is a type  $\gamma$  event which changes the occupation of an anion and its neighboring cation site. Upon densification, the c.n. of affected sites are updated, particularly the neighboring HfX. The result of DFT calculations demonstrates that the presence of bridging O atoms in the neighborhood of the HfX significantly enhances the rate of desorption of HX at this site. Thus, densification of H<sub>2</sub>O and the resulting increase in the c.n. of the HfX sites means that desorption of the remaining HX is more likely to occur during the oxygen pulse. The net effect is an exchange of X<sup>−</sup> with OH<sup>−</sup>, albeit via an indirect route and with a change in surface location. This process is a combination of structural relaxation and a cooperative effect.

As mentioned earlier, desorption of the last HX from HfX has an activation energy which depends on the c.n. of the cation site. For instance, barriers to desorption of HX from five, six, and seven coordinated Hf(HX) in the cation sites are 1.64, 0.83, and 0.56 eV, respectively. Hence, desorption of this HX is facilitated by densification of a H<sub>2</sub>O molecule to a neighboring anion site, as this causes the c.n. to increase. Desorption of

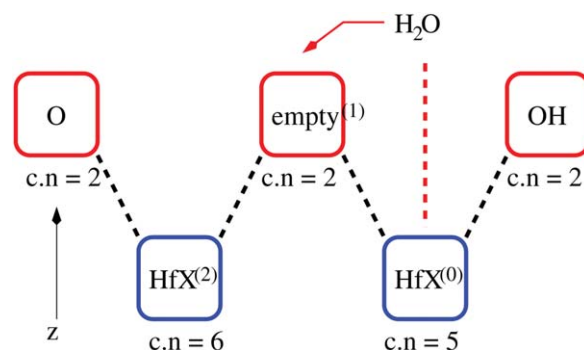


**Figure 9.** Schematic diagram of H<sub>2</sub>O molecule adsorption in two dimensions. H<sub>2</sub>O adsorption occurs in the cation site, due to the presence of another HfX<sup>(2)</sup> at the neighboring cation site (cooperative event). Densification of the H<sub>2</sub>O molecule (red arrow) occurs randomly into an empty anion site  $\square^{(1)}$ . (Same scheme as Fig. 1). [Color figure can be viewed in the online issue, which is available at [wileyonlinelibrary.com](http://wileyonlinelibrary.com).]

the last ligand from seven or eight coordinated HfX leaves Hf in the cation site with bulk-like coordination to O.

### H<sub>2</sub>O migration

After adsorption of a H<sub>2</sub>O molecule, it is densified into an empty anion site, chosen randomly. In most cases, the adsorbed H<sub>2</sub>O molecule is quickly dissociated by neighboring oxygen atoms to yield OH + OH (subsection H<sub>2</sub>O decomposition). These oxygen are usually strongly basic. However, in some cases, the H<sub>2</sub>O molecule densifies to a low coordinated anion site and so becomes attached to fewer Hf atoms. As with HfX<sub>2</sub> migration above, migration of H<sub>2</sub>O is introduced so as to allow the molecule to escape from such less favorable sites. This event is type  $\gamma$ . Activation energies for migration of a water molecule from anion to cation sites depend on the c.n. achieved as a result of densification: 0.43, 0.83, and 1.20 eV, respectively for one, two, and three coordinated H<sub>2</sub>O. However, when migration of the H<sub>2</sub>O molecule is removed from the reaction list, the effect on the growth rate and quality of film is found to be insignificant. We conclude that the difference between random densification and densification incorporating H<sub>2</sub>O migration is negligible.

### H<sub>2</sub>O decomposition

Results of DFT calculations show that the densified H<sub>2</sub>O molecule is easily dissociated by the loss of H<sup>+</sup> to basic oxygen or nitrogen atoms. In order to include this in KMC model, the H<sub>2</sub>O molecule is decomposed into OH + OH due to the existence of under-coordinated oxygen at a neighboring anion site  $\square^{(2)}$  (type  $\beta$ ). Figure 10 shows how the proton of densified H<sub>2</sub>O can be abstracted by oxygen at neighboring anion sites. DFT calculations show that only one or two coordinated oxygen can dissociate the H<sub>2</sub>O molecule, and that the dissociation rate strongly depends on the c.n. of the neighboring anion site. This reaction was not observed for more highly coordinated oxygen neighbors (c.n. = 3 or 4).

### H<sub>2</sub>O desorption

An adsorbed H<sub>2</sub>O molecule decomposes due to the existence of adjacent Lewis bases (low coordinated oxygen, c.n. = 1 or



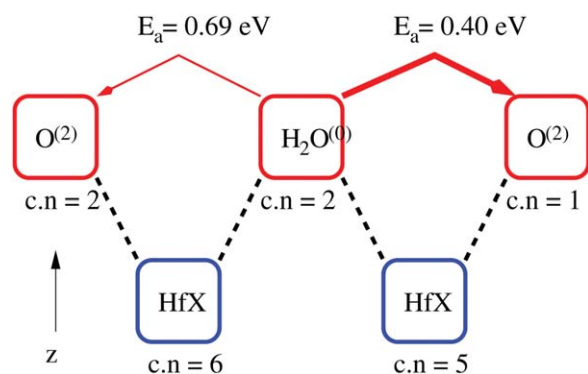


**Figure 10.** Schematic diagram of  $\text{H}_2\text{O}$  molecule decomposition in two dimensions. The activation energies for proton transfer are specified by the different c.n. of the two oxygen neighbors. The thicker arrow indicates stronger attraction by one coordinated oxygen to abstract a proton from  $\text{H}_2\text{O}$ . (Same scheme as Fig. 1). [Color figure can be viewed in the online issue, which is available at [wileyonlinelibrary.com](http://wileyonlinelibrary.com).]

2). In the absence of Lewis basic sites, it remains as a molecule of  $\text{H}_2\text{O}$  and can possibly desorb from the system. *Ab initio* MD shows that desorption of a  $\text{H}_2\text{O}$  molecule happens more read-

ily than desorption of the metal precursor. No other process for desorption of oxygen is considered here, as the other O-containing fragments are charged ( $\text{O}_2^-$ ,  $\text{OH}^-$ ,  $[\text{OHfX}]^+$  etc.). NEB calculations show that an activation energy of 0.46 eV is required to detach  $\text{H}_2\text{O}$  with c.n. = 1 for O (excluding H) from fully coordinated hafnium with c.n. = 7 and 0.83 eV for that from c.n. = 6. Such energy barriers can be easily overcome during the ALD process, especially if the temperature is increased. This event is type  $\alpha$ .

### Neglected reactions

As every site of the anion sublattice is connected to three or four cation sites, through densification oxygen can obtain up to c.n. = 4 to Hf over the span of the oxygen pulse. We consider oxygen with c.n. = 3 or 4 as bulk-like oxygen. However, some of the oxygen remains one or two coordinated to Hf. One-coordinated oxygen (possibly with H) is the active sites for adsorbing  $\text{HfX}_4$  in the next pulse. The activation energy computed with DFT for hopping of O or OH after densification

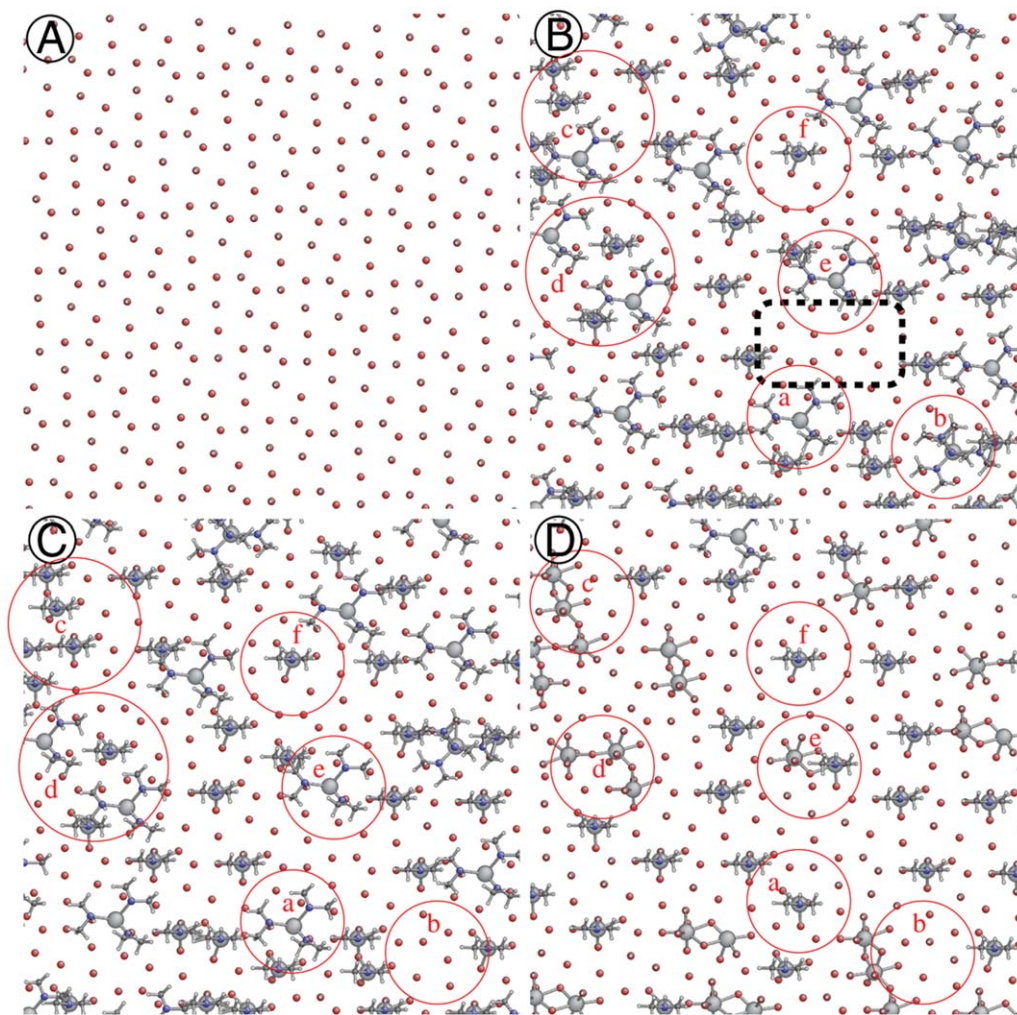


**Figure 11.** Top view of the surface evolution during the first cycle. Snapshots show: (A) The substrate which includes two layers of oxygen (O and OH groups). (B) The end of the metal pulse with a surface that is depleted of protons due to the desorption of HX. (C) The end of the purge with a minor amount of further desorption. (D) The end of the oxygen pulse in which the arrival of  $\text{H}_2\text{O}$  molecules causes oxygen and protons to be introduced to the surface. Fragments for discussion (a–f) are highlighted by circles. The dashed box shows an area where adsorption of the next metal precursor is blocked because of the steric effect.

is too high to be significant for low temperature ALD. Hence, in the present study, oxygen and OH diffusion are ignored.

Following adsorption of a  $\text{H}_2\text{O}$  molecule, densification or decomposition into OH groups may occur. However, no evidence was observed by DFT of two hydroxyl groups recombining again to produce a  $\text{H}_2\text{O}$  molecule. Therefore, this recombination reaction is not considered in our KMC model.

The final type of reactions to be neglected were CVD-like reactions. These are known to be a significant component of  $\text{HfO}_2$  growth from alkylamide precursors. We expect that the inclusion of CVD-like reactions would increase the growth rate. However, in the current calculations, the growth achieved by pure ALD reactions only is reported.

## Results and Discussion

The dimensions of the simulation cell are  $5.8 \times 5.8 \times 6.8$  nm. The cell can contain 20 (111) layers of bulk monoclinic  $\text{HfO}_2$  in the z-direction. Every (111) layer of  $\text{HfO}_2$  includes 256 sites for

Hf (cation sites) and 512 sites for O (anion sites) which will become occupied during the simulation.

Figure 11 shows the top view of the evolution of the surface during the first ALD cycle. Growth begins from an ideal situation in which the substrate is saturated with a regular array of OH groups (Fig. 11A). The initial surface cell is constructed so as to consist of 256 O (c.n. = 2 or 3) atoms and 256 OH groups (c.n. = 1, for O excluding H). It was assumed that these highly coordinated oxygen (c.n. = 2 or 3) are attached to hafnium atoms of a sublayer beyond the cell. Figures 11B–11D are snapshots taken at the end of the first metal precursor pulse time, at the end of the purge time, and at the end of the first oxygen pulse time, respectively. The pulse and purge times are both set at 0.1 ms.

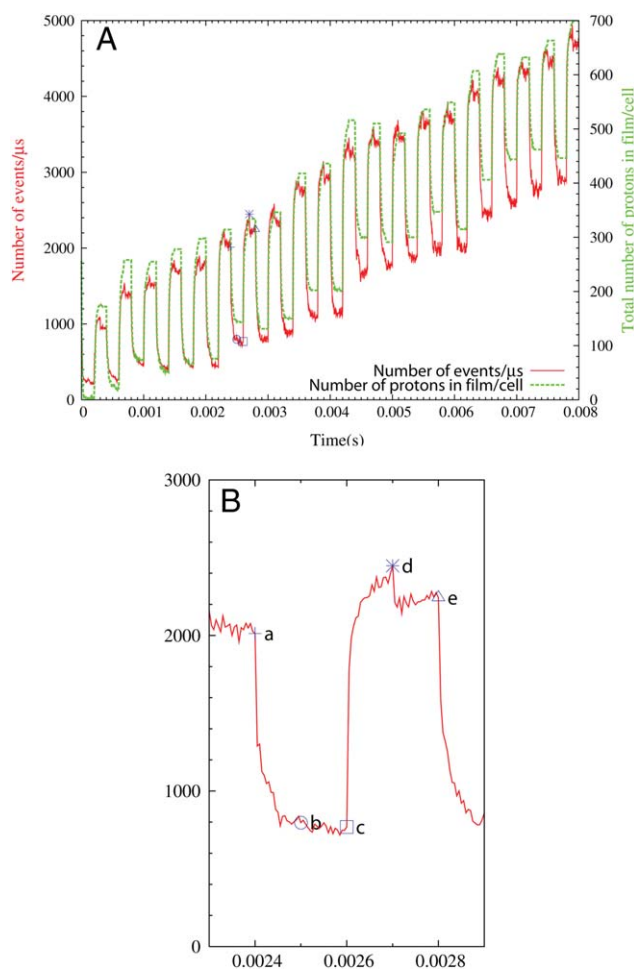
During the metal pulse, protons are observed to “bounce” frequently between the surface oxygen and the nitrogen of the  $\text{HfX}_4$  or  $\text{HfX}_3$  or  $\text{HfX}_2$ . These diffusion events continue in time until all the remaining nitrogen of a precursor fragment has become protonated (multiple proton diffusion). In this situation, desorption of HX is facilitated<sup>[6]</sup> and different species (the remaining fragments) can be seen at the surface, see Figure 11. We have carried out alternative KMC simulations where multiple proton diffusion is switched off and single-proton diffusion is followed by HX desorption with slow kinetics. No evidence of growth is observed in these simulations at 500 K.

In  $\text{H}_2\text{O}$  pulses, the remaining ligands are desorbed from the surface and replaced with OH groups. The net effect is deposition of bulk-like  $\text{HfO}_2$  leaving an  $\text{OH}^-$  terminated surface for the following cycle. An average of  $0.6 \pm 0.02$  Å/cycle of  $\text{HfO}_2$  is deposited in each cycle. Growth is observed simultaneously in multiple layers rather than a single smooth layer in each cycle. An average of  $8.6 \times 10^7$  events is executed in each cycle. In total, over 200 reaction types are considered in reaction list. Simulation of 40 cycles takes approximately 34 h on one central processing unit (CPU).

Our simulations show that the population of surface species changes with temperature. The presence of different species changes the reaction pathways and their associated activation energies, impacting the growth rate. In this situation, owing to the change of activation energies, a longer pulse time should be considered at low temperature and surface saturation is achieved more rapidly at high temperature. In this study, saturation is obtained with the pulse and purge time both set at 0.1 ms. No further adsorption of  $\text{HfX}_4$  is observed by choosing to use a longer pulse time (i.e., 0.2 ms) at  $T = 500$  K. Hence, exposure of both precursors to the surface is set to 27 L. The exposure of precursor and comparison with experiment will be the subjects of our future article.

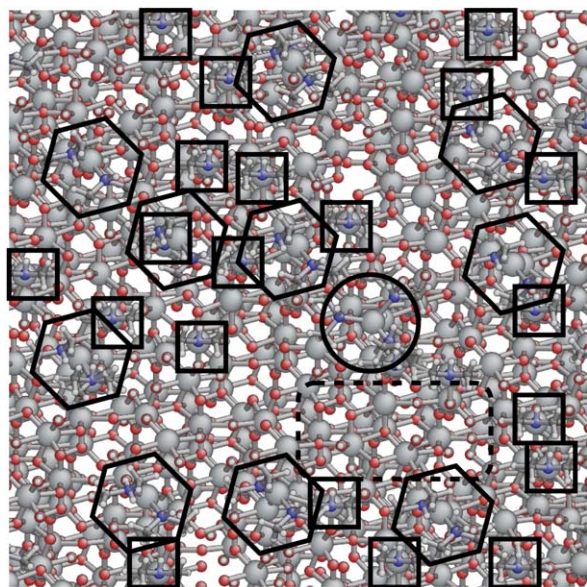
### The metal precursor pulse

Figure 11B shows the fragments remaining after one metal precursor pulse. Due to the ALD reactions, desorption of ligands as HX has occurred. The surface has become depleted of protons. The remaining  $\text{HfX}_3$ ,  $\text{HfX}_2$ , and  $\text{HfX}$  fragments at the surface prevent further adsorption of  $\text{HfX}_4$ , that is, the surface is saturated. For instance, between species 2a and 2e, there are low coordinated substrate oxygen atoms, but insufficient space for adsorption of the metal precursor to occur. The



**Figure 12.** (A) Proton population in film and number of events for 20 cycles. Pulse and purge time have been both fixed at 0.1 ms and temperature is 500 K. Proton population and number of events increase constantly due to the accumulation of protons in the subsurface layers. (B) (a) Start of metal pulse (cycle), (b) start of purge, (c) start of oxygen pulse, (d) start of purge, and (e) end of cycle. [Color figure can be viewed in the online issue, which is available at [wileyonlinelibrary.com](http://wileyonlinelibrary.com).]





**Figure 13.** Top view of the surface at the end of the 18th metal pulse.  $\text{HfX}_3$ ,  $\text{HfX}_2$ , and  $\text{HfX}$  are highlighted by circle, hexagon, and square, respectively. The dashed box shows free space where adsorption of  $\text{HfX}_4$  does not occur. The O and OH groups in the dashed box are highly coordinated or blocked by the remaining ligands. [Color figure can be viewed in the online issue, which is available at [wileyonlinelibrary.com](http://wileyonlinelibrary.com).]

proton population in the film as a function of time is shown for 20 cycles in Figure 12. Desorption of  $\text{HX}$  is visible as a sharp decrease in the proton population at the start of each metal pulse. Correlated with this, there is a sharp decrease in the number of events at the beginning of each metal pulse.

The proton concentration remains low up to the start of the oxygen pulse (Fig. 11C). Dissociation of the  $\text{H}_2\text{O}$  molecule supplies a source of protons for renewed  $\text{HX}$  desorption. Hence, many of the remaining ligands are eliminated (Fig. 11D). At the beginning of the oxygen pulse, an increase in the number of events is observed (Fig. 12). This corresponds to an increase

in the proton population, introducing many proton diffusion events between oxygen atoms.

The number of protons in the film increases constantly during subsequent ALD cycles (Fig. 12). Those protons remain in the layers below the surface. This is unclear whether this is an artifact of our KMC scheme or whether it matches experiment. The protons can undergo proton diffusion reactions within the sublayers but, without access to X, there is no effect on growth. These events are, therefore, wasteful of CPU time. For instance, the CPU time per cycle increases by a factor of 1.5 between the 5th cycle and 40th cycles, almost entirely due to unproductive diffusion of protons in sublayers. Those protons can be observed as OH groups in the dashed box of Figure 13, which shows the end of the metal pulse after 18 cycles. Those OH groups are highly coordinated or blocked. Despite the free space around them, adsorption of the next metal precursor does not take place.

During the metal pulse, ALD reactions (particularly desorption of  $\text{HX}$ ) are decreased, owing to the depletion of the  $\text{H}^+$  coreagent. The number of events, which depends on H and X, is decreased. Interactions between the remaining precursors prevent further adsorptions. However, the self limiting nature of ALD is not solely a consequence of depletion of coreagent. As highlighted in Figure 13 (dashed box), depletion of active sites also prevents further adsorptions. In addition, inert  $\text{HfX}$  and  $\text{HfHX}$  fragments (square) resist desorption of the final ligand, regardless of  $\text{H}^+$  concentration.

All energetically accessible remnants of the Hf precursor ( $\text{HfX}_4$ ,  $\text{HfX}_3$ ,  $\text{HfX}_2$ , and  $\text{HfX}$ ) can be observed at the end of metal pulse, which we now discuss. One  $\text{HfX}_4$  can be seen in Figure 11B-b and this species is desorbed intact during the purge (Fig. 11C) as there are not enough protons in its neighborhood to protonate its ligands. The  $\text{HfX}_4$  population changed from  $0.14 \text{ nm}^{-2}$  at the end of the first cycle to zero at the end of 18th cycle.

$\text{HfX}_3$  is the other species that is often seen during the initial cycles. This species is highlighted in a, e, c, and d (Fig. 11B). If there are insufficient protons in the neighborhood of the adsorbed  $\text{HfX}_4$ ,

then the product is  $\text{HfX}_3$  rather than  $\text{HfX}_2$ . This is because desorption of  $\text{HX}$  from  $\text{HfX}_3$  is more difficult than from  $\text{HfX}_4$ .<sup>[6]</sup> This species has been observed less in later cycles than in first cycles. For instance, the  $\text{HfX}_3$  population changed from  $0.62 \text{ nm}^{-2}$  at the end of the first metal pulse to only  $0.02 \text{ nm}^{-2}$   $\text{HfX}_3$  at the end of the 18th metal pulse (circle in Fig. 13).

$\text{HfX}_2$  is not visible in the snapshots of the first cycle shown (Fig. 11) although it is an important intermediate during KMC. This is because its lifetime is too short here. However, in the next cycles,  $\text{HfX}_2$  does appear at the

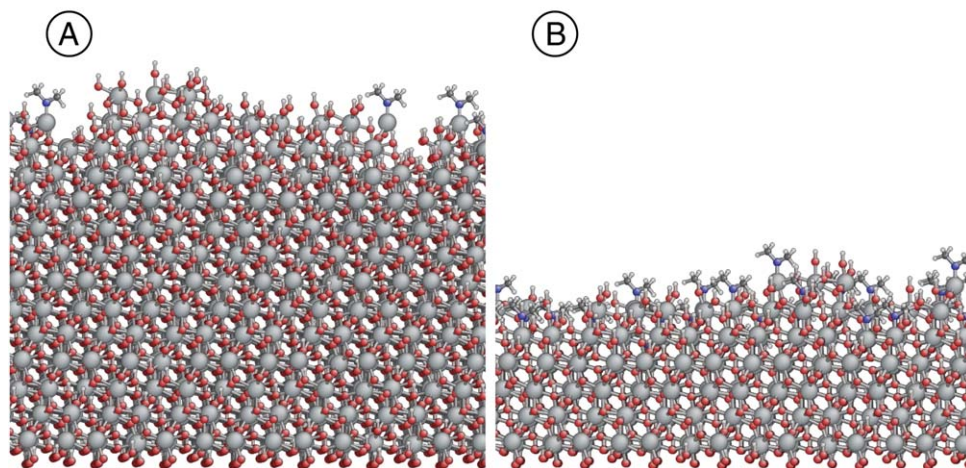


**Figure 14.** Side view of ALD growth for  $\text{HfO}_2$  after 20 cycles. (A) Direct adsorption of  $\text{H}_2\text{O}$  molecules through  $\text{HfX}$  is considered (cooperative effect is neglected). As a result, the growth rate is overestimated by a factor of 2 that obtained when including the cooperative effect only. (B) Cooperation between the  $\text{HfX}$  is considered to adsorb  $\text{H}_2\text{O}$  molecule. [Color figure can be viewed in the online issue, which is available at [wileyonlinelibrary.com](http://wileyonlinelibrary.com).]

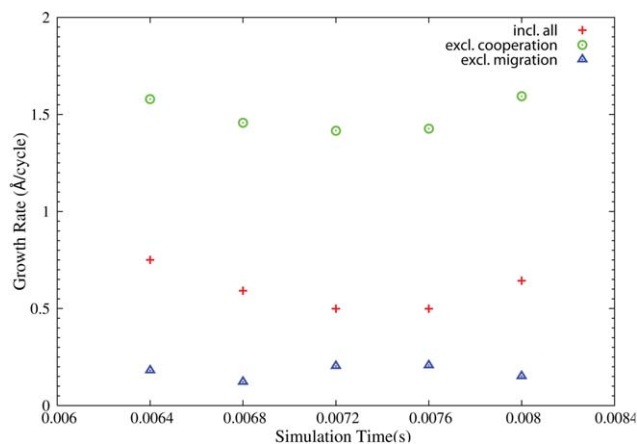


**Figure 15.** Growth rate of  $\text{HfO}_2$  in different circumstances versus time for the 16th–20th cycles. The thickness of a monolayer of  $\text{HfO}_2$  is 2.8 Å. Cross shows growth rate considering all observed ALD reactions. Circle shows growth rate when direct ligand exchange during oxygen pulse is considered rather than cooperative effect. Triangle shows growth rate when migration process is switched off. [Color figure can be viewed in the online issue, which is available at [wileyonlinelibrary.com](http://wileyonlinelibrary.com).]

surface and lasts longer. For instance, the  $\text{HfX}_2$  population is  $0.59 \text{ nm}^{-2}$  at the end of the 18th metal pulse (Fig. 13 hexagon), which is much higher than that in the first cycle. The Hf in these  $\text{HfX}_2$  are always three or four coordinated.

We now discuss the reasons for the persistence of  $\text{HfX}_2$  in later cycles. If through the densification process Hf becomes highly coordinated (c.n.  $\geq 5$ ), ALD reactions will continue rapidly until the remaining fragment is  $\text{HfX}$ . In Figures 13 and 11B-a, the dominant configuration is  $\text{HfX}$ . However, if Hf remains under coordinated (c.n.  $< 5$ ), despite the densification process, the migration event occurs. In this case, the  $\text{HfX}_2$  population is constant while this species diffuses slowly across the surface (referred to as “crawling”). Crawling will continue until the precursor remnant densifies into a cation site with a higher c.n. ALD reactions will then occur rapidly on the remaining fragment of  $\text{HfX}_2$ , until it terminates at  $\text{HfX}$  again, ultimately resulting in a smooth and dense film (Figs. 16B and 14B).

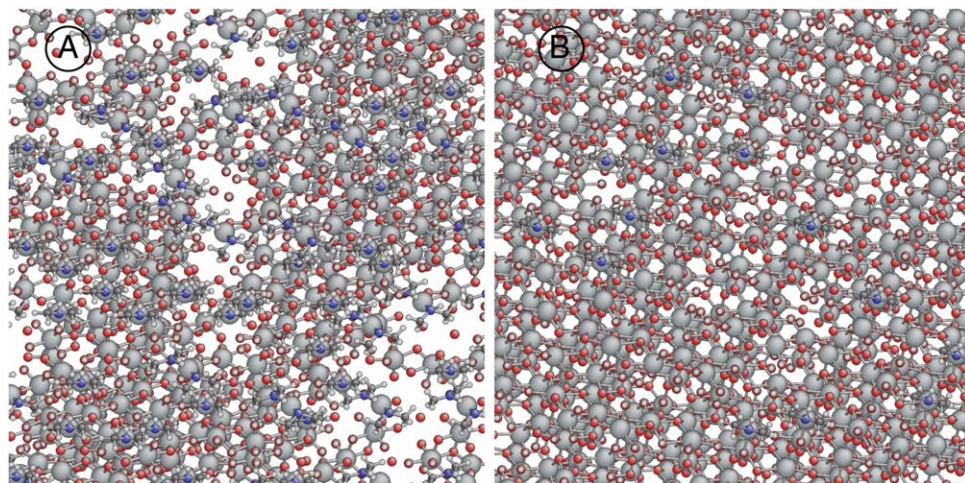


**Figure 16.** Top view of ALD film growth for  $\text{HfO}_2$  after 20 cycles. (A) Migration is removed from the reaction list; a low growth rate and poor quality of film is obtained. (B) Structural relaxation events are considered; a realistic growth rate and dense film are achieved. [Color figure can be viewed in the online issue, which is available at [wileyonlinelibrary.com](http://wileyonlinelibrary.com).]

The growth rate for the 16th–20th cycles of ALD is reported in Figure 15. When all the ALD reactions are considered, the growth rate varies between 0.49 and 0.75 Å/cycle. This simulation includes both cooperative effect and structural relaxation (densification and migration). These KMC growth rates are in excellent agreement with experimental results considering that no parameters were fitted to experiment.<sup>[31–33]</sup> For example, a growth rate of 0.78 Å/cycle is reported by Cho et al.<sup>[31]</sup> at 300°C.

In order to examine the effect of  $\text{HfX}_2$  migration on the growth rate in KMC, the migration process was turned off. Turning this migration off resulted in a growth rate that varies between 0.12 and 0.20 Å/cycle for the 16th–20th cycles (Fig. 15). In other words, excluding the migration causes a low growth rate and poor quality of growth (Fig. 16A).

In spite of migration being allowed, Hf in the remaining  $\text{HfX}_2$  fragment sometimes does not obtain a high enough c.n. and remains three or four coordinated. In those situations, dissociation of  $\text{HX}$  does not happen, even though there are suitable protons at the surface (Fig. 13, dotted box). The system becomes trapped in a set of adjacent local minima (superbasin), where migration happens repeatedly, with no net effect, other than wasting CPU time.

$\text{HfX}$  species are the dominant species at the growing surface at the end of metal pulse [Figs. 11B and 13 (square)]. For instance, the  $\text{HfX}$  population changes from  $1.51/\text{nm}^{-2}$  at the end of first cycle to  $1.42/\text{nm}^{-2}$  and  $1.90 \text{ nm}^{-2}$  at the end of the 18th and 20th cycles, respectively. Such variation may be correlated with the cycle-to-cycle variation in growth rate.

### The purge time

When ALD reactions self-terminate, the remaining ligands block the surface and this persists into the purge step. We have examined our KMC simulations to see if further surface reactions are taking place during the purge. For instance in Figure 11B-c, we see that some  $\text{HfX}_3$  remains at the surface because there are not enough protons in its neighboring sites. After a period of time

during the purge, due to longer-range proton diffusion across oxygen atoms, all nitrogen atoms of these  $\text{HfX}_3$  fragments become protonated and some of them desorb as  $\text{HX}$ . Then, the remnant densifies to the neighboring  $\text{HfX}$  (Fig. 11C-c). This illustrates that slow proton diffusion and associated reactions such as desorption of  $\text{HX}$  continue during the purge time. Indeed, Figure 12 shows that reaction events (mainly proton diffusion) continue at roughly the same frequency during both purges, with just a small decrease over time. This decrement corresponds to the minor desorption during the



purge time. Of course, a longer pulse duration would allow this desorption to occur during the pulse instead of during the purge.

The KMC simulations thus illustrate that fast reactions saturate quickly, whereas slow reactions take orders of magnitude longer. This disparity may explain experimental saturation curves and the difficulty in choosing the optimum pulse/purge time.

### The water precursor pulse

Chemisorption of the  $\text{H}_2\text{O}$  molecule onto a Lewis acidic surface of Hf is a necessary first step for dissociation of the  $\text{H}_2\text{O}$  molecule. Individual Hf have low acidity when bound to a ligand X like  $\text{N}(\text{CH}_3)_2$ . However, we have found that the  $\text{H}_2\text{O}$  molecule can adsorb through cooperation between a cluster of HfX fragments.<sup>[6]</sup> Such a cluster can be seen in Figure 11C-c, where five HfX are in close proximity. In Figure 11D-c, all of these X ligands have been replaced with OH groups. The cluster in Figure 11C-d undergoes a similar reaction to Figure 11D-d. The lifetime of molecular  $\text{H}_2\text{O}$  is too short for it to be observed frequently during the simulation.

By contrast, isolated HfX that is not part of a cluster cannot undergo ligand exchange during the oxygen pulse (Fig. 11D-f). We have attempted running the KMC model with direct ligand exchange at isolated HfX rather than in a cluster and we observe that the growth rate increases to 1.41–1.59 Å/cycle, over twice that obtained when only the cooperative effect is included (Fig. 15). A side view of the simulation box for this direct exchange simulation is shown in Figure 14A.

As indicated in Figure 11C-c, creation of a cluster of HfX during the metal pulse is statistically probable. The necessity of the cooperative effect for adsorption of a  $\text{H}_2\text{O}$  molecule, discussed energetically before,<sup>[6]</sup> is shown quantitatively in KMC. Dissociation of the  $\text{H}_2\text{O}$  molecule creates active sites (OH groups) for the next cycle, as seen in Figure 11D-c.

Incoming protons from dissociation of  $\text{H}_2\text{O}$  molecules in the clusters (e.g., Fig. 11D-c) cause nitrogen atoms in the remaining ligands to become protonated (Fig. 11C-d). Hence, two  $\text{HfX}_3$  lose their remaining ligands to become HfX and densify into the surface. Then, those HfX create a cluster such as Figure 11C-c, during the oxygen pulse. The lifetime of this intermediate is short and, therefore, it is not visible in this snapshot. Ligand exchange immediately happens through the reaction pathway presented for Figure 11D-c, causing the final HX desorb, leaving an  $\text{OH}^-$  terminated surface (Fig. 11D-d).

As well as delivering protons, dissociation of  $\text{H}_2\text{O}$  molecules will also deliver oxygen to the surface. The new oxygen atoms become highly coordinated as the number of remnant ligands decreases, and so these oxygen atoms are densified into the surface and subsurface layers resulting in a dense film. As a result, further desorption of the remaining ligands is facilitated. However, if the incoming oxygen atoms are poorly coordinated, then they become the active sites for the next Hf pulse.

The incoming protons from the dissociation of  $\text{H}_2\text{O}$  also cause desorption of the remaining ligands. The  $\text{HfX}_3$  fragment in Figure 11C-a at the end of the purge loses HX until it terminates as HfX in Figure 11D-a at the end of the oxygen pulse. As there is no HfX at the neighboring sites, in the case of Figure 11D-a as well as 4f, the metal precursor terminates in HfX at the end of

the cycle. This is significantly different from the simple/common assumption that all ligands are eliminated in every ALD cycle. The case illustrated in Figure 11C-e is slightly different. Desorption of HX results in densification of the metal precursor to a pre-existing HfX neighbor. One of the Hf atoms obtains sufficient c.n. from the densified oxygen by dissociation of the  $\text{H}_2\text{O}$  molecule at this site. Further desorption of HX occurs from this cluster and fully coordinated Hf does not cooperate to adsorb a further  $\text{H}_2\text{O}$  molecule. Hence, another HfX present in the cluster remains under-coordinated in Figure 11D-e.

In each cycle, the “freshly deposited” fragments of Hf precursor are usually widely spaced, rather than in clusters, due to the steric bulk of the precursor. Therefore, creation of a cluster of HfX may not happen during a single cycle. However, metal precursors arriving during the next metal pulse may combine with pre-existing HfX to create clusters. These clusters are active sites for adsorption of  $\text{H}_2\text{O}$  molecules such as those shown in Figure 11C-c. In this way, almost all ligands are eventually eliminated over many cycles. Moreover, the ALD growth continues simultaneously in different layers and, therefore, a cluster may be created that spans multiple layers.

### Conclusions

In this study, we develop a 3D on-lattice KMC model to describe the ALD reactions for growth of  $\text{HfO}_2$  from  $\text{Hf}(\text{N}(\text{CH}_3)_2)_4$  and  $\text{H}_2\text{O}$ . We implement all reactions that had been observed in first principles calculations<sup>[6]</sup> as discrete events in the on-lattice KMC simulation. The fundamental chemistry of ALD and its dependence on the local environment at the surface are implemented using c.n. and neighbor list. This includes all steps, from the early stage of adsorption of each ALD precursor, kinetics of the surface protons, interaction between the remaining precursors (steric effect), influence of remaining fragments on adsorption sites (blocking), densification of each ALD precursor, migration of each ALD precursor, and cooperation between the remaining precursors to adsorb  $\text{H}_2\text{O}$  (cooperative effect). Without any fitted parameters, the resulting simulations show the growth of smooth and conformal thin film at growth rates in agreement with experiment.

We propose the migration of the low coordinated precursor fragments (here  $\text{HfX}_2$ ) over areas with a low population of surface oxygen. This process introduces a slow motion (crawling) in the mesoscale. The validity of this and other proposed reaction pathways (e.g., multiple proton diffusion) is statistically established in the mesoscale.

The formation of one monolayer of precursor fragments—crucial for ALD—and the statistical distribution of the remaining fragments is shown at the end of the metal pulse. Adsorption and dissociation of  $\text{H}_2\text{O}$  in clusters of adsorbed HfX are described, leading to the delivery of oxygen and protons to the surface during the oxygen pulse. Through these processes, the remaining ligands desorb from the surface, leaving the surface with bulk-like  $\text{HfO}_2$  terminated by OH for the next cycle. However, creation of a cluster of HfX may not happen during a single cycle. Therefore, we speculate that some isolated HfX does not desorb from the surface at the end of oxygen pulse and persists for multiple cycles instead.

The number of reaction events correlates strongly with the number of protons in the film. The kinetics of the surface

protons are effective in leading to ligand desorption. Proton transfer is the dominant reaction in the event list. Depletion of protons during the metal pulse and delivery of protons during the oxygen pulse cause alternately a decrease and then an increase in the number of events. Some of the introduced protons persist in the bulk and do not participate in the ALD reaction leading to waste of CPU time.

ALD growth is observed to occur simultaneously in different layers. In this way, the inherent roughness of the growth process can be quantified, which is another key property of ALD.

## Acknowledgments

The authors acknowledge the SFI/HEA Irish Centre for High-End Computing (ICHEC) for the provision of computational facilities and support. The authors thank Dr. Kevin Berwick for critically reading the manuscript and his constructive comments. They also thank Dr. A. Esteve, Dr. M. Djafari Rouhani, and Dr. C. Mastail for their instructive discussion.

**Keywords:** density functional theory · kinetic Monte-Carlo · atomic layer deposition · chemical vapor deposition

How to cite this article: M. Shirazi, S. D. Elliott. *J. Comput. Chem.* **2014**, *35*, 244–259. DOI: 10.1002/jcc.23491

- [1] A. O'Mahony, S. Monaghan, R. Chiodo, I. Povey, K. Cherkaoui, R. Nagle, E. O'Connor, R. Long, V. Djara, D. O'Connell, F. Crupi, P. K. Hurley, and M. Pemble, *ECS Trans.* **2010**, *33*, 69, Available at <http://ecst.ecsdl.org/content/33/2/69.full.pdf+html>, <http://ecst.ecsdl.org/content/33/2/69.abstract>.
- [2] P. K. Hurley, E. O'Connor, S. Monaghan, R. Long, A. O'Mahony, I. M. Povey, K. Cherkaoui, J. MacHale, A. Quinn, G. Brammertz, M. Heyns, S. Newcomb, and V. V. Afanas'ev, *ECS Trans.* **2009**, *25*, 113, Available at <http://ecst.ecsdl.org/content/25/6/113.full.pdf+html>, <http://ecst.ecsdl.org/content/25/6/113.abstract>.
- [3] T. Hirvikorpi, M. Vh-Nissi, A. Harlin, M. Karppinen, *Thin Solid Films* **2010**, *518*, 5463, ISSN 0040-6090, Available at <http://www.sciencedirect.com/science/article/pii/S0040609010005407>.
- [4] V. Miikkulainen, M. Leskela, M. Ritala, R. L. Puurunen, *J. Appl. Phys.* **2013**, *113*, 021301, Available at <http://link.aip.org/link/?JAP/113/021301/1>.
- [5] R. A. Adomaitis, *Chem. Vap. Depos.* **2011**, *17*, 353, ISSN 1521-3862, Available at <http://dx.doi.org/10.1002/cvde.201106922>.
- [6] M. Shirazi, S. D. Elliott, *Chem. Mater.* **2013**, *25*, 878, Available at <http://pubs.acs.org/doi/pdf/10.1021/cm303630e>, <http://pubs.acs.org/doi/abs/10.1021/cm303630e>.
- [7] R. Puurunen, *Chem. Vap. Depos.* **2003**, *9*, 249, ISSN 1521-3862, Available at <http://dx.doi.org/10.1002/cvde.200306265>.
- [8] M. A. Alam, M. L. Green, *J. Appl. Phys.* **2003**, *94*, 3403, Available at <http://link.aip.org/link/?JAP/94/3403/1>.
- [9] S. D. Elliott, *Langmuir* **2010**, *26*, 9179, Available at <http://pubs.acs.org/doi/pdf/10.1021/la101207y>, <http://pubs.acs.org/doi/abs/10.1021/la101207y>.
- [10] Z. Hu, J. Shi, C. H. Turner, *Mol. Simul.* **2009**, *35*, 270, Available at <http://www.ingentaconnect.com/content/tandf/gmos/2009/00000035/0000004/art00002>.
- [11] M. D. Groner, F. H. Fabreguette, J. W. Elam, S. M. George, *Chem. Mater.* **2004**, *16*, 639, Available at <http://pubs.acs.org/doi/pdf/10.1021/cm0304546>, <http://pubs.acs.org/doi/abs/10.1021/cm0304546>.
- [12] A. Voter, In *Radiation Effects in Solids*, Vol. 235, NATO Science Series; K. Sickafus, E. Kotomin, B. Uberuaga, Eds.; Springer: Netherlands, **2007**; pp. 1–23, ISBN 978-1-4020-5293-4.
- [13] J. Amar, *Comput. Sci. Eng.* **2006**, *8*, 9, ISSN 1521-9615.
- [14] C. Battaile, D. J. Srolovitz, *Annu. Rev. Mater. Res.* **2002**, *32*, 297, Available at <http://www.annualreviews.org/doi/pdf/10.1146/annurev.matsci.32.01210>, <http://www.annualreviews.org/doi/abs/10.1146/annurev.matsci.32.012102.110247>.
- [15] K. Reuter, First-Principles Kinetic Monte Carlo Simulations for Heterogeneous Catalysis: Concepts, Status, and Frontiers; Wiley-VCH Verlag GmbH and Co. KGaA: Weinheim, **2011**; pp. 71–111, ISBN 9783527639878, Available at <http://dx.doi.org/10.1002/9783527639878.ch3>.
- [16] I. Neizvestny, N. Shwartz, Z. S. Yanovitskaja, A. Zverev, *Comput. Mater. Sci.* **2006**, *36*, 36, ISSN 0927-0256, Proceedings of the Second Conference of the Asian Consortium for Computational Materials Science—ACCMS-2, Second Conference of the Asian Consortium for Computational Materials Science, Available at <http://www.sciencedirect.com/science/article/pii/S0927025605001989>.
- [17] A. Dkhissi, A. Esteve, C. Mastail, S. Olivier, G. Mazaleyrat, L. Jeloica, M. D. Rouhani, *J. Chem. Theory Comput.* **2008**, *4*, 1915, Available at <http://pubs.acs.org/doi/pdf/10.1021/ct8001249>, <http://pubs.acs.org/doi/abs/10.1021/ct8001249>.
- [18] R. J. Bartlett, M. Musiał, *Rev. Mod. Phys.* **2007**, *79*, 291, Available at <http://link.aps.org/doi/10.1103/RevModPhys.79.291>.
- [19] J. Greer, *J. Comput. Phys.* **1998**, *146*, 181, ISSN 0021-9991, Available at <http://www.sciencedirect.com/science/article/pii/S0021999198959538>.
- [20] F. El-Mellouhi, N. Mousseau, L. J. Lewis, *Phys. Rev. B* **2008**, *78*, 153202, Available at <http://link.aps.org/doi/10.1103/PhysRevB.78.153202>.
- [21] K. Reuter, D. Frenkel, M. Scheffler, *Phys. Rev. Lett.* **2004**, *93*, 116105.
- [22] D. T. Gillespie, *J. Phys. Chem.* **1977**, *81*, 2340, Available at <http://pubs.acs.org/doi/pdf/10.1021/j100540a008>, <http://pubs.acs.org/doi/abs/10.1021/j100540a008>.
- [23] G. Mazaleyrat, A. Esteve, L. Jeloica, M. Djafari-Rouhani, *Comput. Mater. Sci.* **2005**, *33*, 74, ISSN 0927-0256, Proceedings of the E-MRS 2004 Spring Meeting; Symposium H: Atomic Materials Design: Modelling and Characterization, E-MRS 2004 Spring Meeting, Symposium, Available at <http://www.sciencedirect.com/science/article/pii/S0927025604003416>.
- [24] A. Bortz, M. Kalos, J. Lebowitz, *J. Comput. Phys.* **1975**, *17*, 10, ISSN 0021-9991, Available at <http://www.sciencedirect.com/science/article/pii/0021999175900601>.
- [25] A. Chatterjee, A. F. Voter, *J. Chem. Phys.* **2010**, *132*, 194101, Available at <http://link.aip.org/link/?JCP/132/194101/1>.
- [26] S. Plimpton, C. Battaile, M. Chandross, L. Holm, A. Thompson, V. Tikare, G. Wagner, E. Webb, X. Zhou, C. G. Cardona, A. Slepoy, Crossing the Mesoscale No-Man's Land via Parallel Kinetic Monte Carlo; Sandia Report, **2009**, sandia national laboratories albuquerque, USA.
- [27] A. Slepoy, A. P. Thompson, S. J. Plimpton, *J. Chem. Phys.* **2008**, *128*, 205101, Available at <http://link.aip.org/link/?JCP/128/205101/1>.
- [28] X. Zhao, D. Vanderbilt, *Phys. Rev. B* **2002**, *65*, 233106, Available at <http://link.aps.org/doi/10.1103/PhysRevB.65.233106>.
- [29] G. Henkelman, B. P. Uberuaga, H. Jonsson, *J. Chem. Phys.* **2000**, *113*, 9901, Available at <http://link.aip.org/link/?JCP/113/9901/1>.
- [30] S. D. Elliott, G. Scarel, C. Wiemer, M. Fanciulli, G. Pavia, *Chem. Mater.* **2006**, *18*, 3764, Available at <http://pubs.acs.org/doi/pdf/10.1021/cm0608903>, <http://pubs.acs.org/doi/abs/10.1021/cm0608903>.
- [31] M. Cho, H. B. Park, J. Park, S. W. Lee, C. S. Hwang, G. H. Jang, J. Jeong, *Appl. Phys. Lett.* **2003**, *83*, 5503, Available at <http://link.aip.org/link/?APL/83/5503/1>.
- [32] L. Nyns, A. Delabie, J. Swerts, S. Van Elshocht, S. De Gendt, *J. Electrochem. Soc.* **2010**, *157*, G225, Available at <http://jes.ecsdl.org/content/157/11/G225.full.pdf+html>, <http://jes.ecsdl.org/content/157/11/G225.abstract>.
- [33] D. M. Hausmann, R. G. Gordon, *J. Cryst. Growth* **2003**, *249*, 251, ISSN 0022-0248, Available at <http://www.sciencedirect.com/science/article/pii/S0022024802021334>.

Received: 24 July 2013  
Revised: 24 October 2013  
Accepted: 30 October 2013  
Published online on 19 November 2013